METHODS

Quantifying Passive Biomechanical Stability Using an Industrial Robot: Development and Experimental Validation of a Task Space Motion Framework

ALEKSANDER SKREDE[1,2], (Graduate Student Member, IEEE), **ANDREAS FAGERHAUG DALEN**[2],
ALF INGE HELLEVIK[2], **ØYVIND STAVDAHL**[3], (Member, IEEE),
AND ROBIN T. BYE[1], (Senior Member, IEEE)

[1]Department of ICT and Natural Sciences, Norwegian University of Science and Technology (NTNU), 6002 Ålesund, Norway
[2]Department of Research and Innovation, Ålesund Hospital Trust, 6017 Ålesund, Norway
[3]Department of Engineering Cybernetics, Norwegian University of Science and Technology (NTNU), 7034 Trondheim, Norway

Corresponding author: Aleksander Skrede (aleksander.l.skrede@ntnu.no)

ABSTRACT This paper presents a methodology and generalized motion framework for quantifying passive biomechanical stability and Range of Motion of human cadaveric specimens, using a position-controlled industrial robot and a wrist-mounted force/torque sensor. Many biomechanical studies on diarthrodial joints using human cadaveric specimens are published in the literature, using various test protocols and machines to apply the loading conditions. In these studies, laxity or mobility of the joints are quantified by measuring the magnitude of translations and rotations with respect to force and torque. The protocols and anatomical motions of the specimens are usually described high-level, textually, and from a medical perspective to a broad audience. The present paper aims to describe, from a technical perspective to a robotics audience, our method to perform biomechanical studies and how existing protocols can be replicated through parameterization using the existing textual descriptions. To accomplish this, we propose a generalized task space motion framework for performing biomechanical studies on diarthrodial joints. The generalization is made by defining the robot Tool Center Point at the cadaveric joint rotation center and aligning the specimen so the anatomical motions can be modeled in world frame or tool frame. The framework was successfully evaluated in a technical pilot study on the shoulder, using one cadaveric shoulder specimen and an established protocol from the literature. The specimen was tested in the intact state and in an injury state, with increased passive instability observed for the injury state compared to intact state.

INDEX TERMS Biomechanics, force control, gradient methods, medical robotics, orthopedic procedures, robotics and automation, robot kinematics, robot motion, shoulder, torque control.

The associate editor coordinating the review of this manuscript and approving it for publication was Kin Fong Lei.

I. INTRODUCTION

Industrial robots are versatile machines that can be adapted to many different processes. Despite their name, they have long been used for non-industrial purposes in healthcare, including research and development within medicine and

biomechanics. Such applications can be post-mortem tissue collection [1] or biopsy [2], osteoporotic hip augmentation [3], assistance in laparoscopic hysterectomy [4], or automated robotic ultrasound imaging [5]. In these applications, the robots assist surgeons with their high durability, precision and accuracy. A related use in the field is robot-assisted surgical research, where robots perform biomechanical tests on human cadaveric specimens [6]. Here, the robots replicate in cadavers one or multiple anatomical motions to measure the joint Range of Motion (ROM), or the robot can apply a force and measure the resulting linear translation. These tests on cadavers can be used to measure the laxity or mobility of the joint, which the robots can perform with better accuracy and better measurements than a surgeon can achieve by hand. Typical objectives in cadaveric biomechanical studies are to study the effect of injury [7], the function of soft tissue structures [8], or the effect of surgical procedures [9].

Many types of machines and robotic devices have been used in cadaveric studies of joint biomechanics. Among these are Stewart platforms [10], cartesian robots [11], material testing machines [12], custom built machines [13] and industrial robots [14]. Whereas these studies use different types of machines to study joint biomechanics, the test protocols and methodology are independent of the machine. The test protocols describe the loading conditions and anatomical positions of the specimens, which can be recreated using any actuating device.

A. RELATED WORK

Fujie et al. [15] appears to be the first to describe a cadaveric biomechanical study using an industrial robot. They described the methodology for studies on the knee, and the mathematical modeling for the loading conditions in their biomechanical tests. They later published a thorough mathematical description for the control and kinematics [16]. This method was expanded by Rudy et al. [17] in a technical note on how to determine forces in a specific ligament in the knee, where they presented a textual description of the kinematics, motion planning and control strategy of the robot. Gilbertson et al. [18] describe a high-level algorithm called PathSEEK for hybrid load-displacement control on human cadaveric spines, based on the work of Fujie et al., where they describe the PathSEEK algorithm visually with textual descriptions of each step.

In the period following these publications, the published cadaveric biomechanical studies appear to be mostly medically focused, until Martínez [19]. He published his thesis on the development of a system for direct robot force control and demonstrated it on the spine. In order to implement direct force control, he modified the robot controller stack and introduced a third-party solution to allow robot joint torque control by increasing the controller cycle rate to 500 Hz. This approach to force control of a position-controlled industrial robot is similar to the approach of Wang et al. [5], which proposed a framework for automated robotic ultrasound imaging.

However, their robot controller had a vendor-provided interface to alter robot joint velocities at 500 Hz.

Since Martínez, more recent technical publications on industrial robots in biomechanics research describe other aspects of the studies, such as accuracy [20], [21], or choice of coordinate systems and approximation of reference frames [22], [23]. Rychlik et al. [24] describe a calibration procedure for estimating the Center of Rotation (COR) of human cadaveric hips, which is applicable to other types of joints.

Hurschler et al. [25] seems to be the first to describe a setup that used an industrial robot and force/torque sensor (FTS) to perform biomechanical tests specifically on the glenohumeral (shoulder) joint. The software and development of their system was described in a habilitation thesis by Hurschler [26], which is not published but was kindly shared with us. This setup was used in several subsequent medical studies on the shoulder, for example as conducted by Wellmann et al. [7] and Schröter et al. [27]. Their protocols varied slightly between studies, but they generally measured glenohumeral stability in the anterior, inferior and anteroinferior directions, as well as external rotation ROM. Recently, their protocol was used to evaluate a novel surgical technique to stabilize the shoulder, described by Klungsøyr et al. [6] and Vagstad et al. [9]. Similar biomechanical studies have been described for the spine [28], hip [22] and knee [29].

There are many published studies on human joint biomechanics using industrial robots. Their use and results are widespread and well documented. However, the technical publications on modeling and control of robots and the specimens to conduct these studies appear to be scarce. Additionally, the technical publications we found on this topic seem to focus on individual cadaveric joint types. Lastly, institutions that facilitates such biomechanical studies, regardless of machine or actuator, seems to either develop their own closed mathematical models and software [6], [22], or use the proprietary and closed source software package called simVITRO® [30]. simVITRO® [31] was designed to perform *in vitro* cadaveric biomechanical studies, and serves both as a middleware and a higher level motion planner for biomechanical studies. The system allows to parameterize protocols and the load profile for the tests and motions.

B. PRESENT STUDY

Goldsmith et al. [20] pointed out that minor differences in the biomechanical test protocol or methodology can produce vastly different results. As such, we argue that the mathematical models for the protocols and actuation must be open and completely described for results to be comparable between studies and institutions. We propose a concise and generalized mathematical description of the kinematics and motion planning, with associated algorithms, as a framework for how to use an industrial robot to perform cadaveric biomechanical studies. Most published biomechanical studies involving industrial robots appears

to be aimed at a very broad audience, and the technical details must be understood by a non-technical audience. Here, we describe for an automation and robotics audience our approach for modeling these biomechanical studies, and how to use our framework to parameterize new or existing biomechanical test protocols. We formulate the mathematics from an algorithmic perspective, with the aim of easy implementation in software, on both new and old robots, without introducing third party solutions or potentially voiding the warranty by modifying the robot controller stack. Our resulting framework is generalized in the sense that it allows one implementation to perform many types of studies based on a set of predefined parameters and algorithms, without altering the underlying control strategy. In future work we will exemplify and describe the generalizability of the framework to other joints. We have partially demonstrated the generalizability of the framework through our medical study on the ankle [32], which utilized our methodology and framework proposed in this paper. The parameterization for the ankle is the topic in a future technical publication currently being drafted.

C. CONTRIBUTION

The method and framework were developed based on our interpretations of the textual descriptions of published biomechanical studies. The contribution of this paper is twofold; (i) a complete and open mathematical framework for parameterizing new or existing biomechanical test protocols, and (ii) the mathematical description and parameterization (replication) of a published biomechanical test protocol for the shoulder. We demonstrate our methodology in (i) using the test protocol in (ii).

D. MOTIVATION

The motivation behind our work was to establish a laboratory to conduct these types of cadaveric biomechanical studies in Norway, and to quickly be able to replicate existing biomechanical studies or test protocols. Additionally, we wish to thoroughly describe our methodology and framework for conducting biomechanical studies, ensuring transparency and facilitating the replicability of our subsequent medically focused studies.

E. STRUCTURE OF THE ARTICLE

Section II provides an overview of the methods and resources used in the present study. Section III describes the modeling approach and the formulation of the cartesian motion framework. Section IV describes how we parameterize the framework for our pilot study. Section V presents the results of the pilot study and a discussion of our chosen strategy. Our concluding remarks are presented in Section VI.

II. MATERIALS AND METHOD
A. MATHEMATICAL NOTATION AND BACKGROUND
Matrix types are denoted using a capital letter whereas vectors are denoted in bold lower-case letters, such as $\boldsymbol{r}$. The

exceptions are vectors representing force ($\mathcal{F} \in \mathbb{R}^3$) or torque ($\mathcal{T} \in \mathbb{R}^3$). Vector components are indexed and in lower-case but not bolded, for example $\hat{\boldsymbol{x}} = \begin{bmatrix} \hat{x}_1 & \hat{x}_2 & \hat{x}_3 \end{bmatrix}^T$. Normal vectors are denoted by a hat, such as $\hat{\boldsymbol{x}}$, whereas estimated values are denoted by a wide hat, such as $\widehat{\boldsymbol{r}}$ or $\widehat{m}$. Parameters of the proposed motion framework are denoted with a left-side superscript p, for example $^P\theta_a$, whereas a left-side superscript s denote parameters related to the parameterization of the shoulder protocol, for example $^s f_l$. See Table 1 at the end of section III for a summary of all framework parameters.

Asterisks in parameters or variables are used to denote that a value has been re-calculated or re-sampled. This has been used in two situations. The first when a variable was re-calculated during the same iteration of the algorithm. The second when distinguishing between values of a variable used in motion planning, and the measured value after executing the motion plan. For example, moving to an angle θ_i about an axis was planned, but during torque control the robot only reached the angle θ_i^*.

Homogeneous transformation matrices were used to represent frames of reference or poses, and rotation matrices were used to represent rotations or orientations. Axis-angle pairs were used to intuitively describe rotations of the specimen. These pairs were converted to rotation matrices [33] which were used to compute target orientations. The rotation matrices for the initial and target orientations were converted to unit quaternions [33], and Spherical Linear Interpolation (SLERP) [34] was used to generate angular trajectories. The rest of this section provides a summary of the mathematical background. Angles are specified in degrees in this paper, but any calculations involving angles must use radians.

Let $(\hat{\boldsymbol{\omega}}, \theta)$ be an axis-angle pair, where $\hat{\boldsymbol{\omega}} \in \mathbb{R}^3$ is the unit vector representing axis of rotation, and $\theta \in \mathbb{R}$ is the angle to rotate about $\hat{\boldsymbol{\omega}}$. The conversion of the axis-angle rotation to matrix form is expressed as shown in (1), where $s = \sin(\theta)$, $c = \cos(\theta)$, $d = \left(1 - \cos(\theta)\right)$ and $\hat{\boldsymbol{\omega}} = \begin{bmatrix} \hat{\omega}_1 & \hat{\omega}_2 & \hat{\omega}_3 \end{bmatrix}^T$.

$$R(\hat{\boldsymbol{\omega}}, \theta) = \begin{bmatrix} \hat{\omega}_1^2 d + c & \hat{\omega}_1\hat{\omega}_2 d - \hat{\omega}_3 s & \hat{\omega}_1\hat{\omega}_3 d + \hat{\omega}_2 s \\ \hat{\omega}_1\hat{\omega}_2 d + \hat{\omega}_3 s & \hat{\omega}_2^2 d + c & \hat{\omega}_2\hat{\omega}_3 d - \hat{\omega}_1 s \\ \hat{\omega}_1\hat{\omega}_3 d - \hat{\omega}_2 s & \hat{\omega}_2\hat{\omega}_3 d + \hat{\omega}_1 s & \hat{\omega}_3^2 d + c \end{bmatrix} \tag{1}$$

The unit quaternion representation, $\boldsymbol{q} \in \mathbb{R}^4$, can be constructed from the axis-angle pair or rotation matrix as shown in (2) and (3).

$$q_0 = \frac{1}{2}\sqrt{1 + R_{11} + R_{22} + R_{33}} = \cos\left(\frac{\theta}{2}\right) \tag{2}$$

$$\begin{bmatrix} q_1 \\ q_2 \\ q_3 \end{bmatrix} = \frac{1}{4q_0} \begin{bmatrix} R_{32} - R_{23} \\ R_{13} - R_{31} \\ R_{21} - R_{12} \end{bmatrix} = \hat{\boldsymbol{\omega}} \sin\left(\frac{\theta}{2}\right) \tag{3}$$

These values form the vector representation of a unit quaternion, $\boldsymbol{q} = \begin{bmatrix} q_0 & q_1 & q_2 & q_3 \end{bmatrix}^T$. Conversion to a rotation matrix, $R \in SO(3)$, is shown in (4), at the bottom of the next page. The interpolation between orientations a and b by using
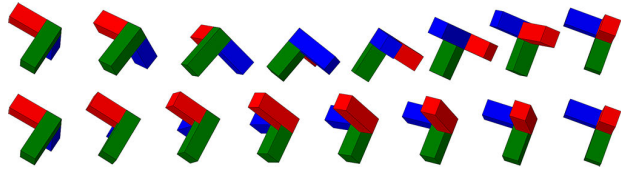
FIGURE 1. Two different angular paths from q_a to q_b. Equations (5)-(6) ensures that the angular path from SLERP yields the shortest path on the geodesic, as shown in the bottom path. Using only the first case in (5), for all q_a and q_b, can produce an undesired angular path that does not follow the shortest path on the geodesic, as shown in the top path.

FIGURE 2. Specimen mounting. (a) Cylinder for the humerus. (b) End-effector adapter. The humerus is potted into the cylinder shown in (a), and is attached to the robot by sliding the cylinder into the adapter shown in (b).

SLERP on the unit quaternion representations is shown in (5).

$$S(\boldsymbol{q}_a, \boldsymbol{q}_b, s) = \begin{cases} S(s-1)\boldsymbol{q}_a + S(s)\boldsymbol{q}_b & , \langle \boldsymbol{q}_a, \boldsymbol{q}_b \rangle < 0 \\ S(1-s)\boldsymbol{q}_a + S(s)\boldsymbol{q}_b & , \text{otherwise} \end{cases}$$

(5)

Here, $0 \le s \le 1$ is the interpolation parameter, $S(\cdot)$ calculates the contribution from each endpoint during interpolation as shown in (6), and θ is the geodesic angle between $\boldsymbol{q}_a$ and $\boldsymbol{q}_b$. This angle can be reused from the axis-angle pair, or calculated as shown in (7) [35], where $\langle \cdot \rangle$ denotes dot product.

$$S(\rho) = \frac{\sin(\rho\theta)}{\sin(\theta)}$$

(6)

The interpolated orientation from $\mathcal{S}$ when $s = 0$ yields the initial orientation a, $s = 1$ the target orientation b, and $s = 0.5$ an orientation half-way on the geodesic. An example path using these equations for angular paths is shown in Fig. 1.

$$\theta = \cos^{-1}\left(2 \cdot \langle \boldsymbol{q}_a, \boldsymbol{q}_b \rangle^2 - 1\right)$$

(7)

B. SOFTWARE AND HARDWARE

A KUKA KR 6 R900 sixx robot and a KUKA KR C4 controller were used in the present study. Kinematics was solved by Trac-IK from Traclabs [36] and motions were generated by an external computer based on the presented framework. Communication between the computer and controller was performed at 250 Hz via the KUKA Robot Sensor Interface. Force and torque were measured using an ATI Gamma FTS. The FTS was calibrated following the process described by Vougioukas [37], and the measurement bias and effects of gravity were subtracted from the FTS measurements.

Visualization of robot motions in Gazebo, as demonstrated in Fig. 4, was used to verify kinematics, reference frame orientations, and modeling of anatomical motions prior to physical testing on specimens. ROS launch files and 3D
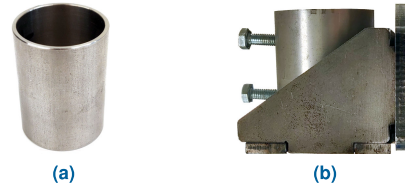
models from the KUKA experimental package[1] were used to set up the Gazebo simulation of the robot, combined with 3D models of the humerus[2] and scapula[3] from UNCG Imaging Lab (under the CC BY 4.0 license[4]).

A fresh frozen cadaveric shoulder specimen without prior injury or surgery was used in the pilot study of the presented framework and protocol. The specimen was thawed for up to 24 hours before being mounted in the test rig. Surgeons performed an osteotomy so that the humerus could be potted in a metal cylinder using a three-component casting resin [38]. The cylinder is shown in Fig. 2. The shoulder specimen was attached to the robot by an end-effector tool adapter inspired by Krämer et al. [38], as shown in Fig. 2b.

The Regional Committees for Medical and Health Research Ethics in Norway approved Vagstad et al. (ref. 2018/2023/REK sør-øst) to use human cadaveric shoulder specimens in biomechanical studies involving robots. The present study underpins this research project and is part of the same approval.

C. BIOMECHANICAL TEST PROTOCOL

This section provides a summary of the biomechanical test protocol used by Vagstad et al. [9], which we aim to replicate by parameterizing our proposed framework. Vagstad et al. evaluated passive biomechanical stability in four different poses of the glenohumeral joint: (i) anatomically neutral, (ii) 60° external rotation, (iii) 60° abduction, and lastly in (iv) 60° abduction and 60° external rotation. In each pose, translation tests were performed in three directions: (i) anterior, (ii) inferior, and (iii) anteroinferior. External rotation ROM tests were performed in 0° abduction and 60° abduction. A 30 N medially oriented force was applied initially to center the humeral head in the glenoid. Then, the translation tests were performed by maintaining the medially oriented force and simultaneously applying 30 N

---

[1] https://github.com/ros-industrial/kuka_experimental
[2] https://skfb.ly/M9SZ
[3] https://skfb.ly/MusD
[4] https://creativecommons.org/licenses/by/4.0/

$$R(\boldsymbol{q}) = \begin{bmatrix} q_0^2 + q_1^2 - q_2^2 - q_3^2 & 2(q_1q_2 - q_0q_3) & 2(q_0q_2 + q_1q_3) \\ 2(q_0q_3 + q_1q_2) & q_0^2 - q_1^2 + q_2^2 - q_3^2 & 2(q_2q_3 - q_0q_1) \\ 2(q_1q_3 - q_0q_2) & 2(q_0q_1 + q_2q_3) & q_0^2 - q_1^2 - q_2^2 + q_3^2 \end{bmatrix}$$

(4)

in the test direction. The referenced protocol constrained motion during translation testing to the medial-lateral axis and test direction. In other words, two of the translation tests (inferior and anterior) required only motion along two axes each. Consequentially for their study, the linear position along the last axis was constant and any arising forces were ignored in that dimension. (We added an emergency stop criteria to our software implementation of the framework to prevent specimen damage, effectively stopping the robot and protocol execution if arising forces or torques got too high compared to the desired force.) The third type of translation test (anteroinferior) required motion along all axes. Lastly, external rotation ROM tests were performed by rotating about the humeral shaft until 2 Nm was achieved.

III. MOTION FRAMEWORK

Our proposed motion framework consists of six parts. The first is (A) the definition of the involved reference frames. The second is (B) the compensation of gravity. The third is (C) the formulation of an implicit force control (force guidance) strategy for linear motions using gradient descent. Force guidance is used to ensure correct cadaveric joint position and to carry out translation tests. The fourth is (D) the angular motions generated using SLERP, and the torque monitoring of these motions for rotation tests and anatomical movement of the specimen. The fifth is (E) a strategy for returning the cadaveric joint to the initial position after force guided motions, by recording and reversing the full path of the motions. Lastly, the sixth is (F) the algorithmic description of the iterations and calculations, using the presented equations. See Table 1 at the end of this section for a summary of the parameters and variables of the framework.

A. REFERENCE FRAMES

The framework requires that the robot end coordinate system, or Tool Center Point (TCP), is located in the COR of the cadaveric joint. For the glenohumeral joint, this is the rotation center of the humeral head. The specimen was mounted so that the anatomically neutral position matched the identity orientation of the TCP, which aligned the anatomical axes and cadaver frame axes with the world frame axes as illustrated in Fig. 3. Then, tests and anatomical motions of the specimen could be modeled as linear and angular motions of the TCP.

The origin in world frame was defined to be in the center of the base of the robot, from which four additional frames in the framework were defined. These frames were fixed to the flange, sensor, adapter, and cadaver, respectively. The transformation matrices used to denote these frames are $T_{wf} \in SE(3)$ from the world frame {w} to the flange frame {f}, $T_{fs} \in SE(3)$ from {f} to the sensor frame {s}, then the two parameterizable frames ${}^{P}T_{sa} \in SE(3)$ from {s} to the adapter frame {a}, and ${}^{P}T_{ac} \in SE(3)$ from {a} to the cadaver frame {c}. The latter two are considered parameters in the framework, as the tool might change with the type of joint, and the cadaver frame changes with each specimen.
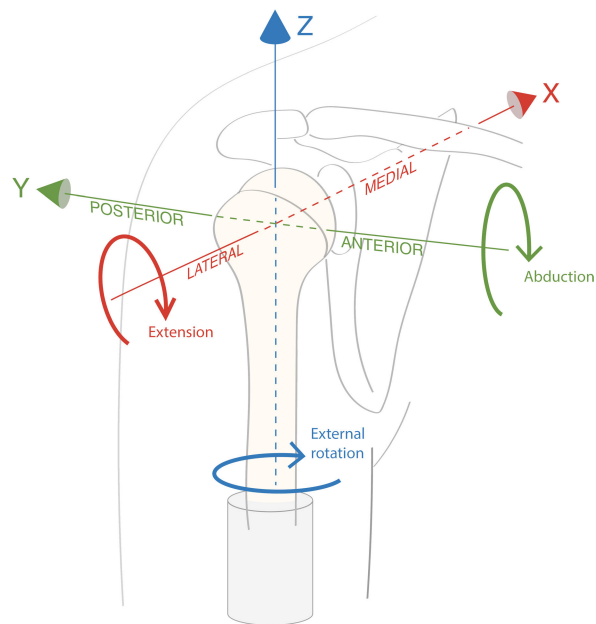

FIGURE 3. Axes of TCP rotation to replicate the anatomical motions of a right-sided shoulder. The cartesian system is in the cadaver reference frame {c} (robot TCP), with origin located in the humeral head COR. In neutral pose of the shoulder, the cadaver frame axes are parallel with the axes of the world frame, {w}. The cartesian and anatomical axes are identical for a left sided-shoulder, except that the anterior-posterior axis is reversed (although, the y-axis remains unchanged).

Forward kinematics was used to calculate T_{wf} based on the robot joint configuration, whereas T_{fs} changes with the FTS. The transformation from the flange frame to the sensor frame is shown in (8). Our sensor was rotated 45° about the flange z-axis due to the layout of custom machined holes of the sensor mounting plate. This was compensated for to align the sensor identity orientation (when $R_{ws} = I_{3\times3}$) with the world frame.

$$T_{fs} = \begin{bmatrix} & & & 0 \\ R(\hat{z}, 45°) & & & 0 \\ & & & 0.033 \\ 0 & 0 & 0 & 1 \end{bmatrix} \quad (8)$$

The structure of the transformation from {s} to {a} for the tool shown in Fig. 2b is given in (9). The offset and orientation of {a} was modeled to ensure the identity orientation of the adapter coincided with the anatomically neutral position of the shoulder. Expressed in the sensor frame {s}, this matrix is stated in (9).

$$^{P}T_{sa} = \begin{bmatrix} & & & 0.044 \\ R(\hat{z}, \pm90°) & & & 0 \\ & & & 0.0335 \\ 0 & 0 & 0 & 1 \end{bmatrix} \quad (9)$$

As seen in the equation, the transformation can take two forms, positive or negative rotation about the z-axis. This was to specify different different poses of the adapter for right-sided and left-sided shoulders in the identity orientation. This was necessary due to the robot mobility and having
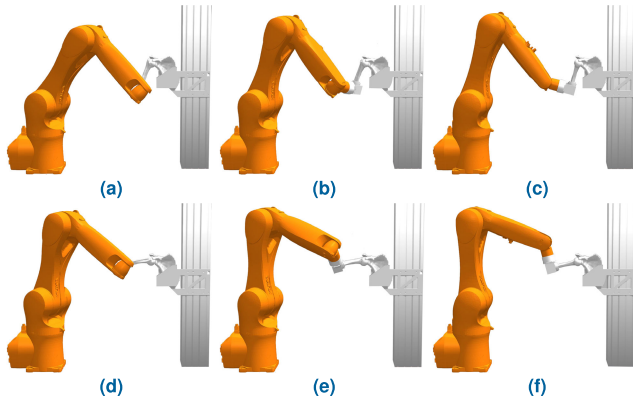
FIGURE 4. Visualizations from Gazebo showing the poses of the robot during abduction and external rotation of a right-sided shoulder. (a) Initial position. (b) 45° external rotation. (c) 90° external rotation. (d) 60° glenohumeral abduction. (e) 60° glenohumeral abduction and 90° external rotation. (f) 60° glenohumeral abduction and 90° external rotation. Relative to (a), (d) shows the rotation for 60° glenohumeral abduction. For a left-sided shoulder, the robot wrist should point out of the page in (a) and (d). Attaching the robot in a pose similar to (c) as a generalization for both right-sided and left-sided specimens would not work, as the robot would not have sufficient ROM for highly mobile specimens to perform the necessary external rotation ROM tests. Notice that joint 4 is rotated close to 180° in (f) compared to (c), which is the limit for our robot model.

to ensure sufficient ROM of the robot to perform external rotation, as illustrated in Fig. 4. In the figure, the flange is pointing into the page, whereas for left-sided shoulders it would be pointing out of the page.

B. GRAVITY COMPENSATION

Compensation for the mass of the specimen must be performed when specimens are supported by the robot, and the overarm rests on the robot in the present shoulder study. The method described by Vougioukas [37] was used to estimate the bias in the force/torque measurements, as well as combined mass and mass center for the sensor and adapter. This compensation method is based on least squares estimation using a series of opposite orientations of the sensor. However, this method cannot be used to estimate the mass and mass center of the overarm, since the robot and specimens form a closed kinematic chain with insufficient ROM to reach the opposite orientations. Instead, we estimated the mass of the specimen in a single pose and used statistical values for the mass center [39].

Let $\mathcal{F}_s \in \mathbb{R}^3$ be the unbiased force measurement and $\mathcal{T}_s \in \mathbb{R}^3$ the unbiased torque measurement, both expressed in the sensor frame $\{s\}$. The gravity compensated measurements in world frame $\{w\}$ can be obtained as stated in (10), where $g_w \in \mathbb{R}^3$ is the vector of gravity in $\{w\}$, $\widehat{m}_s \in \mathbb{R}_{>0}$ the estimated mass attached to the sensor, and $\widehat{r}_s \in \mathbb{R}^3$ the estimated center of the mass in $\{s\}$. Lastly, $R_{ws} \in SO(3)$ is the sensor orientation.

$$\begin{bmatrix} \mathcal{F}_s^* \\ \mathcal{T}_s^* \end{bmatrix} = \begin{bmatrix} \mathcal{F}_s \\ \mathcal{T}_s \end{bmatrix} - \begin{bmatrix} \widehat{m}_s \cdot R_{ws}^T g_w \\ \widehat{m}_s \cdot \widehat{r}_s \times (R_{ws}^T g_w) \end{bmatrix} \quad (10)$$

The sensor measurements expressed in $\{w\}$ can then be obtained as shown in (11).

$$\begin{bmatrix} \mathcal{F}_w \\ \mathcal{T}_w \end{bmatrix} = \begin{bmatrix} R_{ws} \mathcal{F}_s^* \\ R_{ws} \mathcal{T}_s^* \end{bmatrix} \quad (11)$$

Once the specimen was attached to the adapter, the TCP was manually jogged to a pose where the humeral head was slightly lateral of the deepest point of the glenoid. This position was verified by two x-ray images, one with an anterior perspective and one with a superior perspective. The specimen mass was estimated in this pose prior to running the protocol. Let $^{P}m_s \in \mathbb{R}_{>0}$ be the mass of the sensor and adapter as estimated from prior calibration, and $^{P}m_a \in \mathbb{R}_{\geq 0}$ the mass of the specimen attached to the adapter. Then, the total mass estimate for gravity compensation is given in (12).

$$\widehat{m}_s = {}^{P}m_s + {}^{P}m_a \quad (12)$$

Each mass parameter is combined with a mass center parameter. The mass center for the sensor and adapter, as estimated from prior calibration, is denoted by $^{P}r_s \in \mathbb{R}^3$ and expressed in $\{s\}$. Similarly, the cadaver mass center is denoted by $^{P}r_a \in \mathbb{R}^3$ and expressed in $\{a\}$. Then, the total mass center estimate, $\widehat{r}_s \in \mathbb{R}^3$, expressed in $\{s\}$, is given in (13).

$$\begin{bmatrix} \widehat{r}_s \\ 1 \end{bmatrix} = \frac{1}{^{P}m_s + {}^{P}m_a} \left(\begin{bmatrix} ^{P}r_s \\ 1 \end{bmatrix} \cdot {}^{P}m_s + T_{sa} \begin{bmatrix} ^{P}r_a \\ 1 \end{bmatrix} \cdot {}^{P}m_a \right) \quad (13)$$

C. LINEAR MOTION AND FORCE GUIDANCE

Force guidance for linear motion, as described here, refers to an implicit force control strategy, modelled as a modified gradient descent [40] search. This was used to ensure correct joint position and to perform translation tests. The TCP position, $p \in \mathbb{R}^3$, was moved iteratively in world frame in search for the position which minimized the error $\widetilde{\mathcal{F}} \in \mathbb{R}^3$ between a given force setpoint $^{P}\mathcal{F}_u \in \mathbb{R}^3$ and the measured sensor force $\mathcal{F}_w \in \mathbb{R}^3$. The orientation of the TCP was constant.

Let $\mathcal{F}_s$ be the unbiased and gravity compensated force measurement in the sensor frame. The force measurement in world frame, at step t, is given in (14).

$$\mathcal{F}_t = \mathcal{F}_w = R_{ws} \mathcal{F}_s \quad (14)$$

The change in end-effector position between the previous two steps, measured at t, is given in (15),

$$\Delta p_{t-1} = p_{t-1} - p_{t-2} \quad (15)$$

and the change in force between the previous two steps, measured at t, is given in (16).

$$\Delta \mathcal{F}_{t-1} = \mathcal{F}_{t-1} - \mathcal{F}_{t-2} \quad (16)$$

From these, a Jacobian matrix [41] approximation can be constructed for change in position with respect to change in force, as shown in (17). The vectors $\Delta p = \begin{bmatrix} \Delta p_1 & \Delta p_2 & \Delta p_3 \end{bmatrix}^T$

and $\Delta\mathcal{F} = \begin{bmatrix} \Delta\mathcal{F}_1 & \Delta\mathcal{F}_2 & \Delta\mathcal{F}_3 \end{bmatrix}^T$ are calculated as shown in (15) and (16), respectively.

$$J(\Delta\boldsymbol{p}, \Delta\mathcal{F}) = \begin{bmatrix} \frac{\Delta p_1}{\Delta\mathcal{F}_1} & \frac{\Delta p_1}{\Delta\mathcal{F}_2} & \frac{\Delta p_1}{\Delta\mathcal{F}_3} \\ \\ \frac{\Delta p_2}{\Delta\mathcal{F}_1} & \frac{\Delta p_2}{\Delta\mathcal{F}_2} & \frac{\Delta p_2}{\Delta\mathcal{F}_3} \\ \\ \frac{\Delta p_3}{\Delta\mathcal{F}_1} & \frac{\Delta p_3}{\Delta\mathcal{F}_2} & \frac{\Delta p_3}{\Delta\mathcal{F}_3} \end{bmatrix} \quad (17)$$

Lastly, the force error at step t is as shown in (18).

$$\widetilde{\mathcal{F}}_t = {}^p\mathcal{F}_u - \mathcal{F}_t \quad (18)$$

A basic formulation for force guidance using gradient descent can be made as shown in (19), where ζ is the convergence rate and $J_{t-1} = J(\Delta\boldsymbol{p}_{t-1}, \Delta\mathcal{F}_{t-1})$.

$$\boldsymbol{p}_t = \boldsymbol{p}_{t-1} + \zeta \cdot J_{t-1}\widetilde{\mathcal{F}}_t \quad (19)$$

Despite minimizing the force error, notice it appears as an ascent rather than descent due to the addition of the step (instead of subtracting). This is because here we formulated J using position with respect to force. Formulating J using position with respect to force error can be rewritten to (19).

We used an adaptive convergence rate rather than a constant. When pushing bone into bone, such as the humeral head into the glenoid cavity, decreasing increments in position will result in increasing change in contact force. The search strategy can lead to divergence (unstable oscillations and overshoots) which may injure the specimen if the convergence rate is too big, whereas a too small convergence rate will increase the duration of the search. The adaptive convergence rate was calculated by normalizing the computed step and scaling it by a function of the force error. The convergence rate is relatively big for large force errors, and getting smaller as the force error decreases. Here, the convergence rate should be considered as a constrained step size of the TCP rather than a unitless constant. Let ${}^p d \in \mathbb{R}_{>0}$ be the maximum allowed step size of translations, when the force error is big. The constrained step size as a function of force error, $\zeta : \mathbb{R}^3 \rightarrow \mathbb{R}_{>0}$, is then computed as shown in (20), where $a \in \mathbb{R}_{>0}$, $b \in \mathbb{R}_{>0}$ and $c \in \mathbb{R}_{>0}$ are scalar constants, and $\|\cdot\|$ is the Euclidean norm of a vector.

$$\zeta\left(\widetilde{\mathcal{F}}\right) = \frac{{}^p d}{a + b \cdot \exp^{(c - \|\widetilde{\mathcal{F}}\|)}} \quad (20)$$

The constrained step size, ζ, is equal to ${}^p d / a$ when $\|\widetilde{\mathcal{F}}\|$ is large. As $\|\widetilde{\mathcal{F}}\|$ decreases, so do the allowed step size as shown in Fig. 5, which shows. Incorporating this constraint, the guidance equation was modified as shown in (21), compared to (19). Here, $|\cdot|$ denotes vector normalization.

$$\boldsymbol{p}_t = \boldsymbol{p}_{t-1} + \zeta\left(\widetilde{\mathcal{F}}_t\right) \cdot |J_{t-1}\widetilde{\mathcal{F}}_t| \quad (21)$$

Constraining motion to specific frame axes was necessary to perform translation tests. This was achieved by using the Hadamard product of the force error $\widetilde{\mathcal{F}}_t$ and a mask ${}^p\boldsymbol{h} \in \mathbb{B}^3$, in place of the force error in (21). The formulation for linear
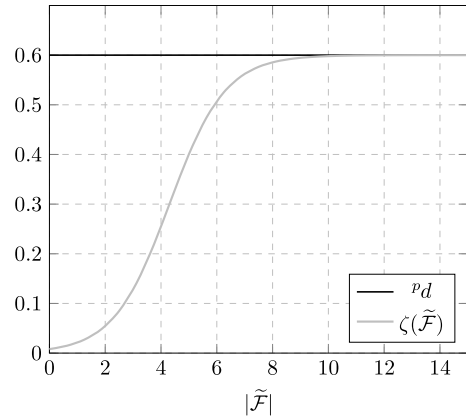

FIGURE 5. Adaptive convergence rate in millimeters as a function of force error, $\widetilde{F}$. The tuning of force guidance convergence rate was performed through modifying ${}^p d$ only, whereas the scalar constants were unchanged. The values ${}^p d = 0.6$, $a = 1$, $b = 10$, and $c = 2$ were found through experimental tuning, using the robot and a shoulder specimen, aiming for stability and relatively fast convergence. Stability in this regard means that the force guided search did not oscillate around the optimal position.

guidance, which incorporates the Hadamard mask, is shown in (22). Here, $\odot$ denotes the Hadamard product.

$$\boldsymbol{p}_t = \boldsymbol{p}_{t-1} + |J_{t-1} \cdot (\widetilde{\mathcal{F}}_t \odot {}^p\boldsymbol{h})| \cdot \zeta\left(\widetilde{\mathcal{F}}_t \odot {}^p\boldsymbol{h}\right) \quad (22)$$

As an example, the Hadamard mask ${}^p\boldsymbol{h} = \begin{bmatrix} 1 & 0 & 0 \end{bmatrix}^T$ constrains motion to the x-axis only. Simply setting the force setpoint to zero in the other dimensions would result in guidance to the force equilibrium for those axes. Instead, any arising forces along the nullified axes were ignored, and the linear position along these axes were kept constant. The mask also ensures the step size calculated from ζ is based on the force error in the active axes only. Constraining the motion during translation testing to specific axes was described in the previously published test protocol we aim to replicate. Ignoring forces along the other axes during force guidance, using the Hadamard mask, is how we achieve motion constraints using our proposed guidance strategy.

This calculation was simplified by not utilizing the partial derivatives in the Jacobian matrix approximation. Our utilized approach can be considered as one-dimensional searches occurring simultaneously along the principal axes. The reason was that this approach converged faster and had less oscillations. The final form of the search equation is shown in (23), where $\oslash$ denotes Hadamard division.

$$\begin{aligned} \boldsymbol{p}_t &= \boldsymbol{p}_{t-1} + |I_{3\times3} \odot J_{t-1} \cdot (\widetilde{\mathcal{F}}_t \odot {}^p\boldsymbol{h})| \cdot \zeta\left(\widetilde{\mathcal{F}}_t \odot {}^p\boldsymbol{h}\right) \\ &= \boldsymbol{p}_{t-1} + |(\Delta\boldsymbol{p}_{t-1} \oslash \Delta\mathcal{F}_{t-1}) \odot (\widetilde{\mathcal{F}}_t \odot {}^p\boldsymbol{h})| \cdot \zeta\left(\widetilde{\mathcal{F}}_t \odot {}^p\boldsymbol{h}\right) \\ &= \boldsymbol{p}_{t-1} + \Delta\boldsymbol{p}_t \end{aligned} \quad (23)$$

This calculation was performed iteratively until the error was below ${}^p f_e \in \mathbb{R}_{>0}$, and the condition in (24) was true.

$$\|\widetilde{\mathcal{F}}_t^* \odot {}^p\boldsymbol{h}\| \leq {}^p f_e \quad (24)$$

D. ANGULAR MOTION AND TORQUE MONITORING

Torque guidance for angular motions is an implicit torque control strategy. The motion was modelled as rotation of the TCP about an axis $^P\hat{\omega}$, from orientation a to orientation b. The path was built using SLERP [34]. This rotation was stopped when the torque setpoint $^P\mathcal{T}_u \in \mathbb{R}^3$ was reached, or the target orientation was reached. The full rotation was divided into intervals, and force guidance was used in between intervals to equilibrate the arising forces due to rotations about a roughly estimated COR. Linear position was constant during rotations.

Torque guidance was used for two purposes. The first was to measure the magnitude of rotation about an axis until reaching a given torque setpoint. The second was to monitor a rotation to a new pose which the specimen was expected to reach, but in theory could be too tight to reach as joint mobility vary.

The axis of rotation, $^P\hat{\omega}$, was one of the principal axes $\hat{x}$, $\hat{y}$ or $\hat{z}$ in either world frame $\{w\}$ or cadaver frame $\{c\}$. Additionally, $^P\hat{\omega}$ also served as the Hadamard mask for comparing the measured torque with the desired setpoint. Let $\mathcal{T}_w \in \mathbb{R}^3$ be the measured torque expressed in the world frame and $\mathcal{T}_c \in \mathbb{R}^3$ expressed in the cadaver frame. Furthermore, let $\mathcal{T}_s$ be the unbiased and gravity compensated torque measurement in the sensor frame. The torque measurement at time t was calculated as shown below.

$$\mathcal{T}_t = \begin{cases} \mathcal{T}_w = R_{ws}\mathcal{T}_s^* & , \text{ world frame} \\ \mathcal{T}_c = R_{sc}^T\mathcal{T}_s^* & , \text{ cadaver frame} \end{cases} \quad (25)$$

Torque arising from force guidance and centering was treated as a bias during rotation tests. The measured torque prior to performing the tests, $\mathcal{T}_{t=0} = \mathcal{T}_0$, was stored and subtracted from subsequent measurements during testing as shown in (26).

$$\mathcal{T}_t^* = \mathcal{T}_t - \mathcal{T}_0 \quad (26)$$

Let $^P\theta_s \in \mathbb{R}_{>0}$ be the angular step size for the interpolation, $^P\theta_a \in \mathbb{R}_{>0}$ the angular distance of the interval, and $^P\theta_r \in \mathbb{R}_{>0}$ the absolute angular distance from the initial orientation R_a about $^P\hat{\omega}$, which is used to calculate R_b as shown in (27).

$$R_b = \begin{cases} R(^P\hat{\omega}, \pm^P\theta_r)R_a & , \text{ world frame} \\ R_aR(^P\hat{\omega}, \pm^P\theta_r) & , \text{ cadaver frame} \end{cases} \quad (27)$$

The list of angular steps for interval i is built in (28) based on the introduced parameters. The number of steps in the interval is denoted by $n_i \in \mathbb{R}_{>0}$, and $\overline{\Theta}_i \in \mathbb{R}_{>0}^{n_i}$ denotes the list.

$$\overline{\Theta}_i = \left\{ \bigcup_{j=1}^{n_i-1} \theta_{i-1}^* + j \cdot {}^P\theta_s \right\} \cup \{\theta_i\} \quad (28)$$

Here, θ_i is the planned angular distance from q_a after the interval i, and θ_{i-1}^* is the angle from q_a to the orientation after the previous interval had stopped. For the first interval, when

$i = 1$, then $\theta_{i-1} = \theta_0 = 0$. The number of orientations in i, n_i, is calculated in (29), where $\lceil \cdot \rceil$ is the ceiling function.

$$n_i = \begin{cases} \left\lceil \dfrac{{}^P\theta_r - \theta_{i-1}^*}{{}^P\theta_s} \right\rceil & , \text{ when } {}^P\theta_r < \theta_{i-1}^* + {}^P\theta_a \\[3mm] \left\lceil \dfrac{{}^P\theta_a}{{}^P\theta_s} \right\rceil & , \text{ otherwise} \end{cases} \quad (29)$$

The last angular step for interval i is calculated as follows.

$$\theta_i = \begin{cases} {}^P\theta_r & , {}^P\theta_r \leq \theta_{i-1}^* + {}^P\theta_a \\ \theta_{i-1}^* + {}^P\theta_a & , \text{ otherwise} \end{cases} \quad (30)$$

The rotation matrices were converted to unit quaternions and SLERP was used to generate the path, $\overline{Q}_i \in \mathbb{R}^{4 \times n_i}$, as shown in (31).

$$\overline{Q}_i = \mathcal{S}\left(q_a, q_b, \frac{\overline{\Theta}_i}{{}^P\theta_r}\right) \quad (31)$$

$$= \left[\mathcal{S}\left(q_a, q_b, \frac{\overline{\Theta}_{i,1}}{{}^P\theta_r}\right) \mathcal{S}\left(q_a, q_b, \frac{\overline{\Theta}_{i,2}}{{}^P\theta_r}\right) \dots \mathcal{S}\left(q_a, q_b, \frac{\overline{\Theta}_{i,n_i}}{{}^P\theta_r}\right) \right]$$

The algorithm for angular motion has three stop conditions. The first was simply if the measured angular distance of the TCP from a was equal to $^P\theta_r$ (if $\theta_i^* = {}^P\theta_r$). The second was based on exceeding the torque setpoint, when (32) held true.

$$\|^P\mathcal{T}_u \odot {}^P\hat{\omega}\| \geq \|\mathcal{T}_t^* \odot {}^P\hat{\omega}\| \quad (32)$$

Then, force guided re-centering was performed to equilibrate any arising forces, and (32) was re-evaluated. If (32) no longer held true and the path was not completed, a new rotation interval was computed and rotation resumed.

The measured angular distance of the final few intervals before converging based on torque was usually significantly smaller than planned. The third finish condition was added based on the angular distance of the $^Pn_\theta \in \mathbb{R}_{>0}$ most recent intervals. If the average distance was shorter than some threshold $^P\Delta\theta_c \in \mathbb{R}_{>0}$, the rotation was considered converged. Let $\Delta\theta_i^* \in \mathbb{R}$ be the angular distance between the intervals i and $i-1$, as calculated in (33).

$$\Delta\theta_i^* = \theta_i^* - \theta_{i-1}^* \quad (33)$$

Then, the list of the previous angular distances of the intervals, $\overline{\Delta\Theta}_i \in \mathbb{R}_{\geq 0}^{{}^Pn_\theta}$, is given as follows.

$$\overline{\Delta\Theta}_i = \left\{ \bigcup_{j=0}^{{}^Pn_\theta} \Delta\theta_{i-j}^* \right\} \quad (34)$$

When the number of intervals was at least $^Pn_\theta$ and the average angular distance of the intervals was at or below the threshold $^P\Delta\theta_c$, the rotation was stopped. The condition is given in (35).

$$\left({}^Pn_\theta \leq i\right) \wedge \left(\frac{1}{{}^Pn_\theta} \sum_{j=1}^{{}^Pn_\theta} \overline{\Delta\Theta}_{i,j} \leq {}^P\Delta\theta_c \right) \quad (35)$$

The relationship between the parameters and values for the planned angular motion is shown in Fig. 6. To summarize,
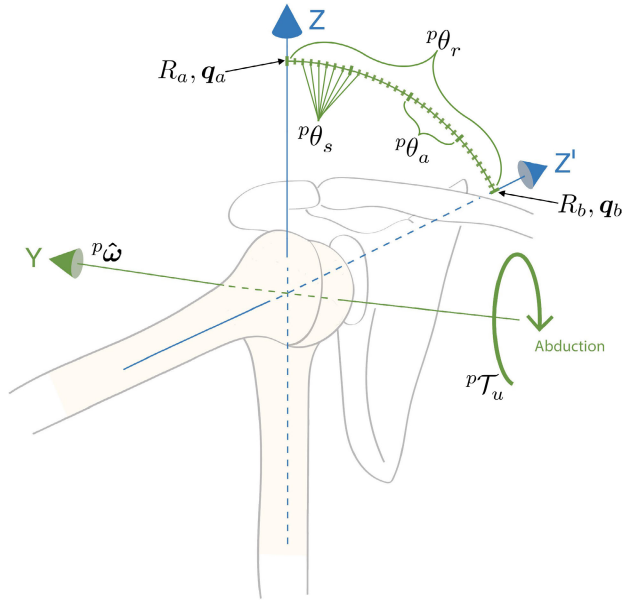
FIGURE 6. Illustration of the torque parameters and variables for replicating the anatomical movement *abduction*. The figure shows 90° glenohumeral abduction by rotating about the y-axis.

TABLE 1. Summary of parameters, constants, and variables of the general motion framework.

Name	$\in$	Unit	Description
T_{wf}	$SE(3)$		Transformation from world frame $\{w\}$ to flange frame $\{f\}$.
T_{fs}	$SE(3)$		Transformation from flange frame $\{f\}$ to sensor frame $\{s\}$.
$^{p}T_{sa}$	$SE(3)$		Transformation from sensor frame $\{s\}$ to adapter frame $\{a\}$.
$^{p}T_{ac}$	$SE(3)$		Transformation from adapter frame $\{a\}$ to cadaver frame $\{c\}$ (joint COR).
$^{p}m_{s}$	$\mathbb{R}_{>0}$	kg	Estimated mass of the sensor and adapter.
$^{p}m_{a}$	$\mathbb{R}_{>0}$	kg	Estimated mass of the specimen.
$^{p}\boldsymbol{r}_{s}$	$\mathbb{R}^{3}$	m	Mass center of $^{p}m_{s}$ in $\{s\}$.
$^{p}\boldsymbol{r}_{a}$	$\mathbb{R}^{3}$	m	Mass center of $^{p}m_{a}$ in $\{a\}$.
$\widehat{\boldsymbol{r}}_{s}$	$\mathbb{R}^{3}$	m	Combined mass center expressed in $\{s\}$.
$^{p}\mathcal{F}_{u}$	$\mathbb{R}^{3}$	N	Force setpoint for guided linear motions.
$\widetilde{\mathcal{F}}$	$\mathbb{R}^{3}$	N	Force setpoint to measurement deviation.
$^{p}f_{e}$	$\mathbb{R}_{>0}$	N	Acceptable magnitude of $\widetilde{\mathcal{F}}$ for converging the force guidance algorithm.
^{p}d	$\mathbb{R}_{>0}$	mm	Highest linear step size in force guidance.
$^{p}d_{o}$	$\mathbb{R}_{>0}$	mm	Linear distance between the preceding and succeeding waypoints for optimization.
$^{p}\boldsymbol{h}$	$\mathbb{B}^{3}$		Hadamard mask for constraining motion along specific principal axes.
R_{a}	$SO(3)$		Start orientation in rotation planning.
R_{b}	$SO(3)$		Target orientation of a full rotation, calculated from R_{a}, $^{p}\widehat{\boldsymbol{\omega}}$, and $^{p}\theta_{r}$.
$^{p}\widehat{\boldsymbol{\omega}}$	$\mathbb{R}^{3}$		Axis of rotation, a principal axis in either world frame or cadaver frame.
$^{p}\theta_{r}$	$\mathbb{R}_{>0}$	°	Angular distance from R_{a} to R_{b} about $^{p}\widehat{\boldsymbol{\omega}}$ for a rotation segment.
$^{p}\theta_{a}$	$\mathbb{R}_{>0}$	°	Angular distance of rotation intervals.
$^{p}\theta_{s}$	$\mathbb{R}_{>0}$	°	Angular step size for rotations.
$^{p}\mathcal{T}_{u}$	$\mathbb{R}^{3}$	Nm	Torque setpoint, or torque limit, for the rotations.
θ_{i}	$\mathbb{R}_{>0}$	°	Planned angular position after interval i.
$\Delta\theta_{i}^{*}$	$\mathbb{R}_{>0}$	°	Measured angular distance after interval i.
n_{i}	$\mathbb{R}_{>0}$		The number of angular steps in interval i.
$\overline{\Theta}_{i}$	$\mathbb{R}^{n_{i}}$	°	The path for interval i as angular steps.
$\overline{Q}_{i}$	$\mathbb{R}^{4 \times n_{i}}$		The path for interval i as quaternions.
$^{p}n_{\theta}$	$\mathbb{R}_{>0}$		The number of intervals required with magnitude below the angular threshold to decide convergence towards the torque setpoint.
$\overline{\Delta\Theta}_{i}$	$\mathbb{R}_{\geq 0}^{^{p}n_{\theta}}$	°	The average angular distance of the previous $^{p}n_{\theta}$ intervals.
$^{p}\Delta\theta_{c}$	$\mathbb{R}_{>0}$	°	Threshold for average angular distance of the previous $^{p}n_{\theta}$ rotation intervals.

the arc in the figure represents the planned rotation from R_{a}. The full motion is divided into intervals with an angular distance of $^{p}\theta_{a}$. The small steps between the intervals are the angular steps, with an angular distance of $^{p}\theta_{s}$. Here, for the anatomical movement *inversion*, the axis of rotation is the world frame y-axis. The depicted arc and intervals do not necessarily reflect the magnitude of the values used during inversion; the image is illustrating the involved parameters and variables.

E. PATH REVERSAL OPTIMIZATION

Force guided paths may visit many positions during the guidance. Instead of guiding the TCP back to the initial position, the original path was recorded and followed in reverse. However, moving through all the explored positions when following the path in reverse is unnecessary and the path can be optimized.

Let $\overline{T}$ be a list of waypoints and $N(\overline{T})$ a function which returns the number of elements in $\overline{T}$. Then, let $O(\overline{T}, i)$ be a recursive function that returns the optimized path, where i denotes the index from where optimization should be performed. If the linear distance between waypoint i and $i + 2$ was smaller than or equal to some specified step size, $^{p}d_{o} \in \mathbb{R}_{>0}$, then waypoint $i + 1$ was removed from the list. The function $O(\overline{T}, i)$ is defined in (36).

$$O(\overline{T}, i) = \begin{cases} \overline{T} & , i = N(\overline{T}) - 1 \\ O(\overline{T} \setminus \{\overline{T}_{i+1}\}, i) & , E(\overline{T}_{i}, \overline{T}_{i+2}) \leq {^{p}d_{o}} \\ O(\overline{T}, i + 1) & , \text{otherwise} \end{cases}$$

(36)

Here, $\overline{T}_{i}$ denotes the i-th element in the list $\overline{T}$, the function $E(\overline{T}_{j}, \overline{T}_{k})$ returns the Euclidean distance in millimeters

$$p_{t=1} = p_0 + |(\widetilde{\mathcal{F}}_t \odot {}^p h)| \cdot \zeta(\widetilde{\mathcal{F}}_t \odot {}^p h)$$

$t = t + 1$

$$p_t = p_{t-1} + \Delta p_t$$

$\|\widetilde{\mathcal{F}}_t^* \odot {}^p h\| \leq {}^p f_e$ false $t = t + 1$

true

Finish
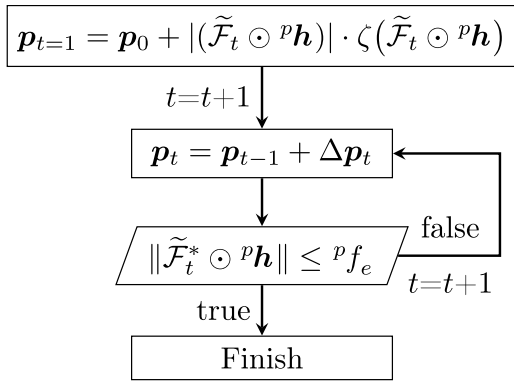
FIGURE 7. The algorithm for force guidance of linear motions.

between the waypoints $\overline{T}_j$ and $\overline{T}_k$, and lastly $\overline{T} \setminus \{\overline{T}_i\}$ denotes list subtraction, where element i is removed from the list $\overline{T}$. The optimized path $\overline{T}_o$ can be calculated based on the force guided path $\overline{T}_g$ as shown in (37), which can be followed in reverse to reach the initial position. The path $\overline{T}_o$ must be reversed.

$$\overline{T}_o = O(\overline{T}_g, 1) \tag{37}$$

F. ALGORITHMIC REPRESENTATION

See Table 1 for a summary of the parameters and variables defined in the framework. The algorithm for force guidance, using the presented equations and parameters, is shown in Fig. 7. Force guidance starts from the initial position of the TCP, denoted by P_0.

Similarly, the algorithm for torque monitored rotations is shown in Fig. 8. As seen, this algorithm has three finish conditions. The first is when the torque setpoint is exceeded after equilibrating the forces, the second if R_b is reached, and third if the average angular distance of the previous ${}^p n_\theta$ rotation intervals is at or below the threshold. The grey box for force guidance represents the algorithm shown in Fig. 7.

IV. PARAMETERIZATION FOR THE SHOULDER

This section describes the parameterization of our framework for replicating the referenced biomechanical shoulder protocol, in preparations for a future study by Vagstad et al. Parameters relating specifically to the shoulder protocol are denoted by a left-side superscript s. Consult Table 1 for a description of the framework parameters, denoted by a left-side superscript p.

The experimental procedure of the implemented shoulder protocol begins by centering the humeral head in the glenoid cavity. The full procedure for the protocol is shown in Fig. 10. Once centered and the linear guidance converged, the test sequence begins for the first pose. A recorded path of the TCP for the initial centering and the force guidance convergence can be seen in Fig. 14. The test sequence consists of three translation tests in each of the four poses, and external rotation ROM test performed in both angles of glenohumeral
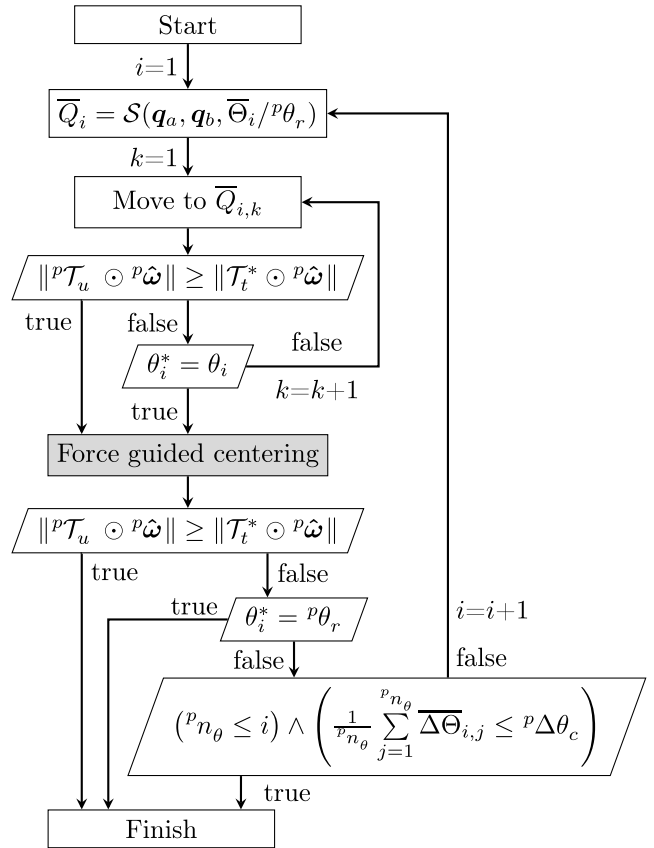
Start

$i = 1$

$\overline{Q}_i = \mathcal{S}(q_a, q_b, \overline{\Theta}_i / {}^p \theta_r)$

$k = 1$

Move to $\overline{Q}_{i,k}$

$\|{}^p \mathcal{T}_u \odot {}^p \hat{\omega}\| \geq \|\mathcal{T}_t^* \odot {}^p \hat{\omega}\|$

true   false $\theta_i^* = \theta_i$ false $k = k+1$

true

Force guided centering

$\|{}^p \mathcal{T}_u \odot {}^p \hat{\omega}\| \geq \|\mathcal{T}_t^* \odot {}^p \hat{\omega}\|$

true   false

true $\theta_i^* = {}^p \theta_r$ $i = i+1$

false   false

$\left({}^p n_\theta \leq i \right) \wedge \left(\frac{1}{{}^p n_\theta} \sum_{j=1}^{{}^p n_\theta} \overline{\Delta \Theta}_{i,j} \leq {}^p \Delta \theta_c \right)$

true

Finish

FIGURE 8. The algorithm for torque monitored angular motions. The grey box performs the algorithm for linear force guidance to equilibrate arising forces between rotation intervals.
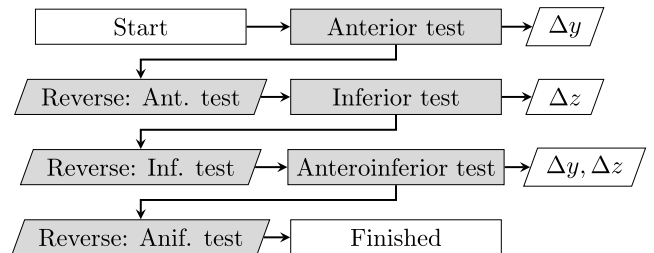
Start → Anterior test → Δy

Reverse: Ant. test → Inferior test → Δz

Reverse: Inf. test → Anteroinferior test → $\Delta y, \Delta z$

Reverse: Anif. test → Finished

FIGURE 9. Experimental procedure for the translation test sequence. This test sequence is performed in each of the four poses of the shoulder. The rectangular boxes in grey performs the force guidance algorithm shown in Fig. 7, using the parameters presented in this section. The rhomboid boxes performs the described path reversal optimization strategy.

abduction (0° and 60°). See Fig. 9 for the performed test sequence in each of the four poses.

A. CADAVER FRAME

The cadaver frame transformation matrix must be defined per specimen, as the humeral osteotomy of specimens can result in different lengths of the humerus. The humeral shaft length, ${}^s H \in \mathbb{R}_{>0}$, from the adapter to the humerus COR was measured using x-ray, while both the medial offset, ${}^s M \in \mathbb{R}_{>0}$, and posterior offset, ${}^s P \in \mathbb{R}_{>0}$, were obtained from statistical values [42]. The transformation from $\{a\}$ to
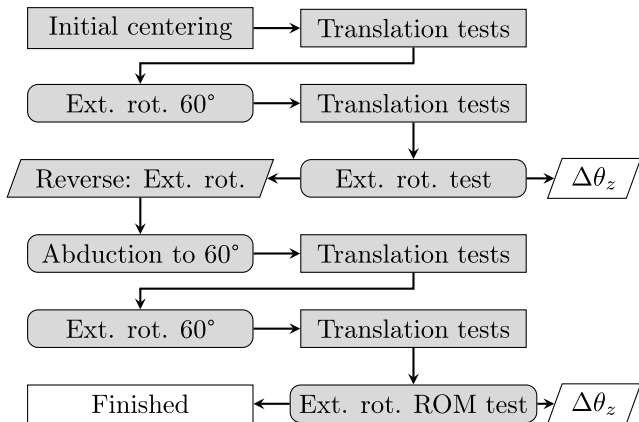
FIGURE 10. The experimental procedure for the test full protocol. The rectangular boxes in grey performs the force guidance strategy, where translation tests specifically is the sub-procedure shown in Fig. 9. The rounded rectangular box performs the torque guidance algorithm shown in Fig. 8 using the parameters presented in this section.
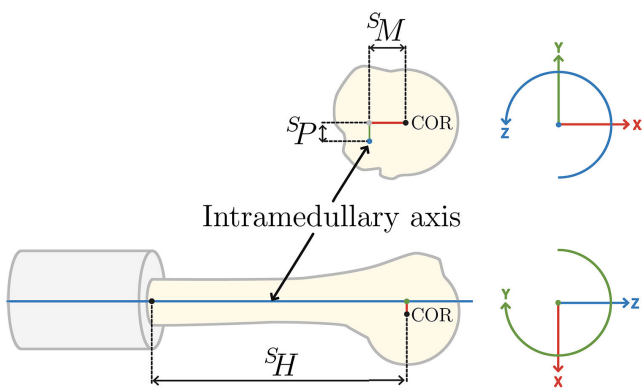

FIGURE 11. Projections of the humerus and coordinate axes onto the xy-plane (superior perspective) and xz-plane (anterior perspective), illustrating the linear offset of the cadaver frame {c} (the humeral COR) relative to the adapter frame {a}.

$\{c\}$ is defined in (38) and illustrated in Fig. 11. This method to define the humeral COR was adapted from Iannotti et al.

$$
{}^{P}T_{ac} = \begin{bmatrix} & & & {}^{s}M \\ I_{3\times3} & & \pm{}^{s}P \\ & & & {}^{s}H \\ 0\ 0\ 0 & & 1 \end{bmatrix} \tag{38}
$$

B. CENTERING
The humeral head was centered in the glenoid cavity by using the linear force guidance strategy described in our framework, using a non-zero medial-lateral (x-axis) force component whereas the inferior-superior (z-axis) and anterior-posterior (y-axis) components were set to zero. The cartesian coordinates relative to the shoulder can be seen in Fig. 3 and Fig. 12. The humeral head may dislocate during centering when there is a surgically made bone defect. If this happened, the protocol was restarted, and a small bias directed away from the injury was added to the force
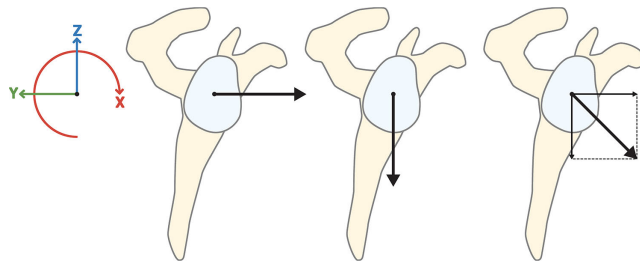

FIGURE 12. Direction of forces for translation tests of a right-sided shoulder. Medial perspective of the shoulder. Left: Anterior test direction. Middle: Inferior test direction. Right: Anteroinferior test direction, composed by anterior and inferior loads.

setpoint. Let ${}^{s}f_{c} \in \mathbb{R}_{\geq0}$ be the magnitude of the medially directed force, whereas ${}^{s}f_{pb} \in \mathbb{R}_{\geq0}$ and ${}^{s}f_{sb} \in \mathbb{R}_{\geq0}$ are the posterior and superior biases, respectively. The bias forces should be as small as possible to have a negligible effect on the centered position, typically ranging between 1 N to 5 N. The parameterization of the centering is then as follows.

$$
\begin{array}{ll}
{}^{s}f_{c} = 30\,\text{N} & {}^{P}f_{e} = 0.25\,\text{N} \\
{}^{P}d = 0.6\,\text{mm} & {}^{P}\boldsymbol{h} = \begin{bmatrix} 1 & 1 & 1 \end{bmatrix}^{T} \\
\end{array} \tag{39}
$$
$$
{}^{P}\mathcal{F}_{u} = \begin{bmatrix} -{}^{s}f_{c} & \pm{}^{s}f_{pb} & {}^{s}f_{sb} \end{bmatrix}^{T}\,\text{N}
$$

The value of the second component in ${}^{P}\mathcal{F}_{u}$ is positive for left-sided shoulders and negative for right-sided shoulders.

C. PATH REVERSAL
To reach the initial centered position after translation tests and ROM tests, all guided paths were recorded, optimized and reversed. The following parameter was used.

$$
{}^{P}d_{o} = 0.25\,\text{mm} \tag{40}
$$

D. TRANSLATION TESTS
Translation tests were performed as force guided motions, with motion constrained to specific axes by different Hadamard masks. Test directions for a right-sided shoulder are illustrated in Fig. 12. Note that the anterior direction is parallel but in opposite direction along the y-axis for left-sided shoulders.

Let ${}^{s}f_{l} \in \mathbb{R}_{\geq0}$ be the magnitude of test force. The following parameterizations were used to replicate the translation tests. Note that the value of the second component in ${}^{P}\mathcal{F}_{u}$, when non-zero, is positive for left-sided shoulders and negative for right-sided shoulders.

1) ALL TESTS

$$
{}^{s}f_{c} = 30\,\text{N} \quad {}^{P}f_{e} = 0.25\,\text{N} \quad {}^{P}d = 0.6\,\text{mm} \quad {}^{s}f_{l} = 30\,\text{N} \tag{41}
$$

2) ANTERIOR TEST

$$
{}^{P}\boldsymbol{h} = \begin{bmatrix} 1 & 1 & 0 \end{bmatrix}^{T}
$$
$$
{}^{P}\mathcal{F}_{u} = \begin{bmatrix} -{}^{s}f_{c} & \pm{}^{s}f_{l} & 0 \end{bmatrix}^{T}\,\text{N} \tag{42}
$$

This test was measured as the absolute displacement along the y-axis, Δy.

3) INFERIOR TEST

$$^p\boldsymbol{h} = \begin{bmatrix} 1 & 0 & 1 \end{bmatrix}^T$$
$$^p\mathcal{F}_u = \begin{bmatrix} -^s f_c & 0 & -^s f_l \end{bmatrix}^T \text{ N} \qquad (43)$$

This test was measured as the absolute displacement along the z-axis, Δz.

4) ANTEROINFERIOR TEST

$$^p\boldsymbol{h} = \begin{bmatrix} 1 & 1 & 1 \end{bmatrix}^T$$
$$^p\mathcal{F}_u = \begin{bmatrix} -^s f_c & \pm^s f_l \frac{1}{\sqrt{2}} & -^s f_l \frac{1}{\sqrt{2}} \end{bmatrix}^T \text{ N} \qquad (44)$$

This test was measured as the absolute displacement along both the y-axis and z-axis, $\sqrt{\Delta y^2 + \Delta z^2}$.

E. ABDUCTION
Abduction was performed as a torque monitored rotation of the TCP about the world y-axis, using the following parameters.

$$\begin{array}{ll}
^p\theta_r = 60° & ^p\theta_a = 3° \\
^p\theta_s = 0.25° & ^p\Delta\theta_c = 0.2° \\
^p n_\theta = 6 & ^p\hat{\boldsymbol{\omega}}_m = \begin{bmatrix} 0 & 1 & 0 \end{bmatrix}^T \\
^p\mathcal{T}_u = \begin{bmatrix} 0 & 2 & 0 \end{bmatrix}^T \text{ Nm} & R_b = R(^p\hat{\boldsymbol{\omega}}_m, {}^p\theta_r)R_a
\end{array} \qquad (45)$$

F. EXTERNAL ROTATION
External rotation was performed as rotations about the cadaver frame z-axis (humeral shaft). The initial pose, R_a, was reused when the ROM test was performed after the translation tests. The ROM tests resumed rotation from 60° external rotation after translation tests and continued until the rotation converged. In case a specimen was unable to reach 60° external rotation, the current orientation was considered as the converged ROM test and translation tests were performed in this pose.

$$\begin{array}{ll}
^p\theta_r = 60° & ^p\theta_a = 3° \\
^p\theta_s = 0.25° & ^p\Delta\theta_c = 0.2° \\
^p n_\theta = 6 & ^p\hat{\boldsymbol{\omega}}_m = \begin{bmatrix} 0 & 0 & 1 \end{bmatrix}^T \\
^p\mathcal{T}_u = \begin{bmatrix} 0 & 0 & 2 \end{bmatrix}^T \text{ Nm} & R_b = R_a R(^p\hat{\boldsymbol{\omega}}_m, \pm^p\theta_r)
\end{array} \qquad (46)$$

The sign of $\pm^p\theta_r$ is positive for left-sided shoulders and negative for right-sided shoulders. The same parameters and constants were used for the ROM test, except that $^P\theta_r = 180°$ and R_b was re-calculated.

V. EXPERIMENTAL RESULTS AND DISCUSSION
A. SHOULDER PROTOCOL
The output of each test in the protocol, as measured by the robot, is shown in Table 2. The unit is degrees for external
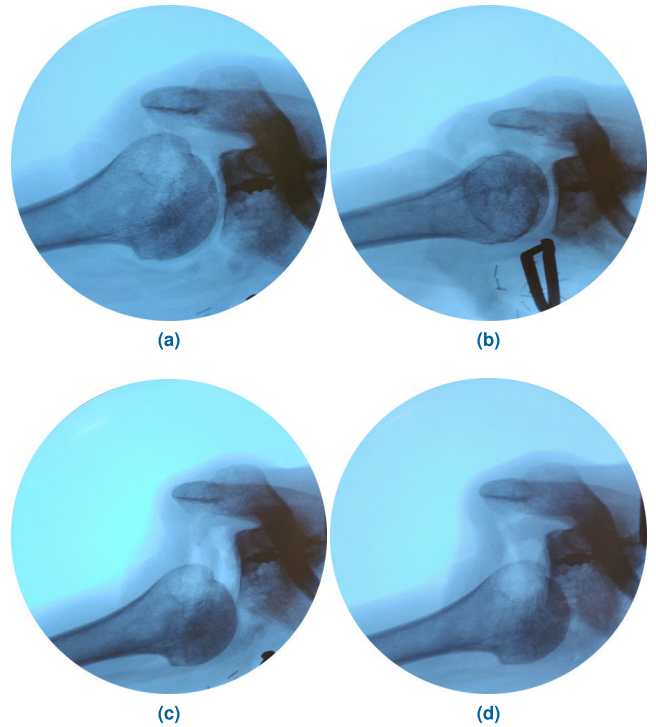

FIGURE 13. X-ray images of the specimen in 60° glenohumeral abduction as guided by the robot. Images are from an anterior perspective. (a) Force centered humeral head. (b) 60° external rotation. (c) Inferior translation test. (d) Anteroinferior translation test.

rotation and millimeters for translations. The first line in the table shows the test results for the intact state, and the second line in the injured state. Poses of the specimen are stated in angles of abduction (ABD) and external rotation (EXR). For example, as 0° ABD / 60° EXR or equivalently as 0° / 60°.

The position of the humeral head was observed using x-ray before and after each test to ensure correct joint position and motion. The humerus as guided by the robot is shown in Fig. 13, where Fig. 13a shows the centered position prior to translation tests and external rotation. Fig. 13b shows 60° external rotation, whereas Fig. 13c shows an inferior translation test and Fig. 13d shows an anteroinferior translation test.

The expectations from the testing were that; (i) the ROM and translations for the injured state should be similar or greater than the intact state, and (ii) the anterior and anteroinferior translations were expected to be largest for 0° / 0° and smallest for 60° / 60°. The assumption behind (i) was that the bony and soft tissue structures that provide passive stability were compromised in the injured state, and (ii) that soft tissue structures tighten and stabilizes the joint during abduction and external rotation.

The observation in Table 2 following our pilot study of the framework, is that each test performed in the injured state measured a greater or similar magnitude compared to the intact state. The tightest pose for the specimen during

TABLE 2. Output from the shoulder test. The first two columns show the output from the external rotation (EXR) ROM tests in different poses of abduction (ABD). The remaining columns show the output of the anterior (ANT), inferior (INF), and anteroinferior (ANIF) translation tests in the four test poses.

0 ABD	60 ABD	0 EXR / 0 ABD			0 EXR / 60 ABD			60 EXR / 0 ABD			60 EXR / 60 ABD		
EXR	EXR	ANT	INF	ANIF	ANT	INF	ANIF	ANT	INF	ANIF	ANT	INF	ANIF
74.38	81.15	5.81	24.09	29.42	5.60	15.82	16.08	5.68	8.99	14.26	4.73	6.71	5.65
77.67	83.84	11.26	29.18	35.18	5.84	24.15	23.71	5.82	13.54	26.52	5.87	8.25	6.84

testing was 60° / 60° for both states. However, the anterior tests in 60° / 0° and 0° / 60° for both states measured similar displacements. The greatest external rotation ROM was observed in 60° glenohumeral abduction, as expected.

A limitation of our pilot study is that statistical significance of the magnitude of motions cannot be decided based on one specimen. However, the present study was not medically focused and did not aim to conclude on the significance of stability or ROM between the intact and injured state. Rather, the present study aimed to develop our framework and demonstrate its use by parameterizing a biomechanical test protocol for the shoulder found in the literature.

B. MOTION FRAMEWORK

Our modeling and control strategy to biomechanical studies is most distinctive through our generalized approach and framework, compared to prior technical descriptions we found in the literature. Our open framework most closely resemble the software solution simVITRO® [31] which is proprietary and, to the best of our knowledge, closed source with a closed model. Other technical descriptions we found in the literature usually describe mathematically the control for specific joints but allow parameterization of the loading conditions. We describe a framework where the anatomical joint motions, biomechanical tests, and the loading conditions can be parameterized without incorporating knowledge of the joint directly in the control strategy.

The model described by Fujie et al. [16] was based on parameterizing the Jacobian matrix approximation using position and force/torque relative to the knee coordinates. They must likely formulate a new Jacobian matrix for other tests or joints. Rudy et al. [17] expanded on this model for other studies on the knee, but we could not find a mathematical description of this adaptation as thorough as the original study. Gilbertson et al. [18] applied the model by Rudy et al. to the spine and proposed the PathSEEK algorithm, describing the parameters and steps of the algorithm textually. The present work combines the mathematical detail by Fujie et al. and the algorithmic description by Rudy et al., and we generalized the methodology and mathematical formulation to be independent of the type of joint. Our approach does not model the Jacobian approximation for loading conditions, or rotations using specimen coordinate systems/specific human joint kinematics, instead we model desired force/torque loading with respect to the world (robot) frame cartesian axes. The generalizability of the framework is a product of the specimen alignment in the rig with respect to the world frame.

Martínez [19] described in his thesis the technical background for a novel application of direct force control of an industrial robot for biomechanical studies. The system was applied on the spine, but he argued it was general and could be applied on other types of joints. A caveat of this approach was that the robot controller stack was altered, introducing third-party solutions to allow robot joint torque control and to increase the controller cycle rate to 500 Hz. Presumably his model can be implemented in robot systems which has these features from the vendor as well. However, we had a KUKA KR 6 R900 sixx available for the present study, which is a joint position-controlled industrial robot and allows external communication at 250 Hz using the KUKA Robot Sensor Interface (RSI). We had no interest in attempting to modify the robot controller stack in the risk of being unable to request official service and support in the future. As such, direct force control as described by Martínez was not a viable option for us, and we opted for an implicit force control strategy.

From the work of Fujie et al. (and subsequent studies by his associates) to Martínez, we have not found any publications on the robot control and modeling in biomechanical studies with the same mathematical detail and generalizability. The work of the former has been used and cited in many ensuing biomechanical studies, and any adaptation of the original work seem to be mostly textually described. Whereas these studies and their descriptions are valuable contributions, replicating both the technical infrastructure and the test protocol using these descriptions is complex and time consuming. Once implemented, our framework may greatly reduce the time to replicate existing test protocols. Additionally, as stated in the introduction, Goldsmith et al. [20] pointed out that minor differences in the test methodology or protocol can produce vastly different results. We observed this during development of the framework and protocol, particularly pertaining to the setpoint/threshold values and convergence strategy to rotations and translations. This is discussed in the next subsection but is tangential to the current discussion; Fig. 15 illustrates this as the convergence rate drops substantially and temporarily at waypoint 10. Consequentially, a high threshold could converge the guidance to a local optimum. This illustrates the importance of open methods, algorithms, and parameters so that differences in results between studies can be explained.

A limitation of the present study is the lack of demonstration of generalizability to other joints. However, as stated in the introduction, we have successfully applied the framework to the ankle joint in our medical study [32]. This demonstrates the generalizability partially, but only to a specific type
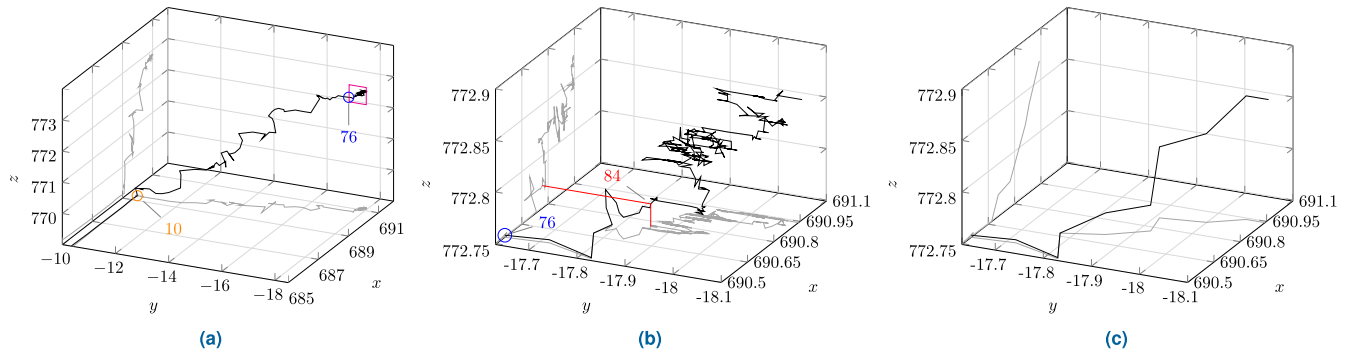
FIGURE 14. Initial force guided centering path of the TCP, consisting of 349 waypoints. Axes show world frame dimensions in mm. After attaching the humerus to the robot, the TCP was jogged manually so that the humeral head was approximately aligned with the glenoid in the superior-inferior and anterior-posterior axes, but lateral to the glenoid so the bones were not in contact. This pose was verified by x-ray prior to centering, and was used for mass estimation of the specimen. (a) The full path of the TCP, and the converging segment shown inside the red box. (b) The converging segment inside the red box. (c) Optimized converging segment, as trimmed by the path reversal method. Note that the entire path was optimized, not just the segment shown here.

of diarthrodial joint; both the shoulder and ankle can be considered to have one point of contact between the bones. Our current formulation of the framework might not be able to replicate anatomical motions in joints with two points of contact, such as the knee. This will be a topic of discussion in our future technical publication that describes our ankle study. Additionally, we only measured the total magnitude of motions during tests, be it linear translation tests or rotations tests, whereas the simVITRO® software package seems to have the ability to log the force-displacement curves and load profiles throughout the motions. This is not implemented in our software for the framework as it was not a requirement for our medical studies, and only the magnitude of motions was of interest. Lastly, our calibration method for the humeral COR was based on x-ray measurements, an alternative could be the method described by Rychlik et al. [24] for the hip.

We have argued that explicit mathematical descriptions for adaptations of subsequent studies is essential, and this is the primary gap that we aimed to close with our presented method. Any adaptations of test protocols in our framework can be directly and explicitly described using the presented set of parameters. We did not modify the underlying control strategy or the framework for our referenced ankle study, but parameterized the framework to adapt an established biomechanical test protocol for the ankle. Our approach to model in task space, using basic mathematical representations and algorithms, has the positive side-effect of being easy to implement on a variety of systems.

C. FORCE GUIDANCE AND PATH OPTIMIZATION

The force guided path of the TCP during the initial centering is shown in Fig. 14a. The red box in the top right of the figure encloses the the converging segment of the path, which is isolated in Fig. 14b. The optimized path of the same converging segment is shown in Fig. 14c. The path starts at

the bottom left of Fig. 14a and visited a total of 349 waypoints (WPs) from start to the converged position. The converging segment in Fig. 14b accounted for 274 WPs, whereas the path outside this box accounted for 75 WPs. The optimized return segment in Fig. 14c only consisted of 10 WPs in contrast to the original 274 WPs in Fig. 14b. For visual reference in this discussion, WPs 10, 76, and 84 are highlighted in their respective figures.

By inspecting the plots, one can see that the TCP travelled approximately 4 mm medially (positive world x-axis) until the humeral head made contact with the glenoid at approximately WP 10. The medial motion at the beginning was the result of the x-component of $\widetilde{F}$ being substantially larger than the other two components. The continued medial travel after WP 10 was due to the humeral head sliding deeper into the glenoid cavity, approximately 2 mm until convergence. Similarly, after WP 10, the TCP traveled approximately 8 mm anteriorly (negative world y-axis) and 4 mm superiorly (positive world z-axis) until convergence. In total, roughly 9.2 mm from WP 10 until convergence.

By rearranging (20) to solve for $|\widetilde{F}|$ when given a value of ζ, the value of the force error magnitude at WP 10 was approximately 2.2 N. This was almost 10 times higher than the threshold, ${}^{s}f_{e} = 0.25$ N, and was one of the smallest steps before WP 84, as illustrated in Fig. 15. After this point, the total distance until convergence was 0.4 mm with all steps smaller than 0.05 mm, and an average step size of 0.017 mm. As such, the average force error was 0.77 N, close to three times the value of ${}^{s}f_{e}$.

There is a trade-off between relatively high and low values of ${}^{s}f_{e}$. Too high and the guidance will converge prematurely, for example in the local minima at WP 10. Consequentially, this would incorrectly have added 8 mm to the value of the anterior translation test in Table 2 (more than doubled the measured motion), as the humeral head was not correctly centered in the glenoid cavity. The other scenario, as potentially demonstrated here, is a too low value
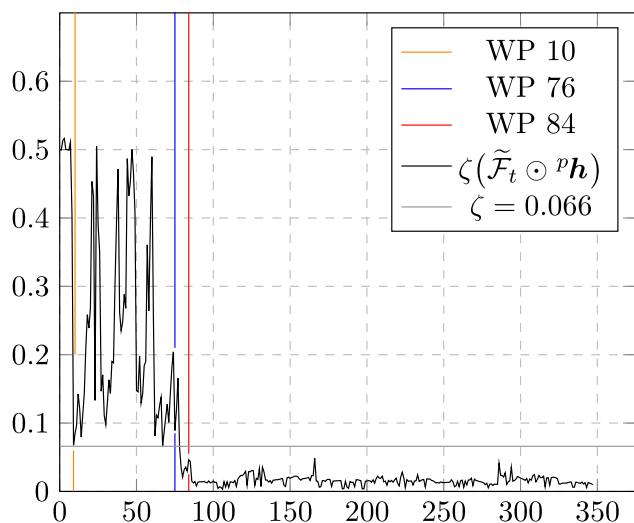
FIGURE 15. The calculated step size (gradient descent convergence ratio) for each waypoint in the path, from the initial centering shown in Fig. 14. The blue bar highlights waypoint 76 in this path, and the red bar waypoint 84.

of the threshold. A too low threshold, presumably, do not negatively affect the outcome of tests but it increases the duration for a potentially negligible difference in position. Related to this, the max step size (or convergence rate), $^{p}d = 0.6\,\mathrm{mm}$, was assigned this specific value to avoid oscillations during centering. This was found experimentally during development using a different specimen than the one included in the pilot study, whereas the values of the constants a, b and c in (20) were found by visual inspection of different plots of ζ. These values were used as listed to avoid a zero-valued root of the function, and were tested experimentally along with the threshold for the force error, $^{s}f_{e}$, during development. These specimens were used in a prior study by Vagstad et al. and had already been injured and surgically repaired. As such they were not suitable to include in the present pilot study. We unfortunately do not have any data from these tests, but the parameter values were kept due to the observed stability and relatively short convergence time in tests during development.

To attempt to reduce the testing time in the future, experiments on multiple specimens should be performed to find proper parameter values. These experiments should include specimens in the intact state and with different injuries. An alternative to experimentally finding different stable values of $^{s}f_{e}$ is to modify the convergence criteria to something similar as for rotations where the last $^{p}n_{\theta}$ steps are observed, or a combination of both. Lastly, to reduce total time, a higher $^{s}f_{e}$ could be used during centering between rotation intervals. During rotations to anatomical positions, it is not important to have the humeral head in the exact anatomically correct position until the rotation is close to convergence. Rather, centering serves to prevent dislocations and to equilibrate arising forces due to the inaccurate COR. Then, centering with a low threshold to ensure correct joint position can be performed during rotation convergence checks, or after the rotation has stopped.

VI. CONCLUSION

This paper presents a modeling method and parameterizable task space motion framework for using a joint position-controlled industrial robot to quantify biomechanical stability and Range of Motion (ROM) of human cadaveric diarthrodial joints. We successfully demonstrated how the framework can be used to parameterize an existing biomechanical test protocol for the shoulder, and evaluated experimentally the replicated protocol in a pilot study. The specimen was tested according to the protocol in the intact state and with anterior glenoid bone loss; the observations generally matched the expectation of increased instability for the injured state. The positions of the humeral head, relative to the glenoid, were validated by an orthopedic surgeon using x-ray before and after all robot-guided motions. Our proposed framework can rapidly recreate existing biomechanical test protocols, or develop new ones. Whereas test protocols are described and published extensively in the literature, we have not found an open and free model equivalent to our framework. The generalizability of the framework to other joints has not been described in this paper, but our proposed framework has been applied in a published cadaveric biomechanical study on the ankle. Thus, the generalizability of the framework to other joints has been demonstrated. The parameterization for the ankle and the extent of the generalizability of the framework are topics in our next technical paper currently being drafted.

REFERENCES

[1] M. Neidhardt, S. Gerlach, R. Mieling, M.-H. Laves, T. Weiß, M. Gromniak, A. Fitzek, D. Möbius, I. Kniep, A. Ron, J. Schädler, A. Heinemann, K. Püschel, B. Ondruschka, and A. Schlaefer, "Robotic tissue sampling for safe post-mortem biopsy in infectious corpses," *IEEE Trans. Med. Robot. Bionics*, vol. 4, no. 1, pp. 94–105, Feb. 2022.

[2] B. Maris, M.-C. Fiazza, M. De Piccoli, C. Tenga, L. Palladino, S. Puliatti, A. Iseppi, R. Ferrari, A. Piro, L. R. Bonetti, G. Ligabue, A. Tafuri, S. Micali, and P. Fiorini, "Preclinical validation of a semi-autonomous robot for transperineal prostate biopsy," *IEEE Trans. Med. Robot. Bionics*, vol. 4, no. 2, pp. 311–322, May 2022.

[3] M. Bakhtiarinejad, C. Gao, A. Farvardin, G. Zhu, Y. Wang, J. K. Oni, R. H. Taylor, and M. Armand, "A surgical robotic system for osteoporotic hip augmentation: System development and experimental evaluation," *IEEE Trans. Med. Robot. Bionics*, vol. 5, no. 1, pp. 18–29, Feb. 2023.

[4] J. Wu, W. Chen, D. Guo, G. Ma, Z. Wang, Y. He, F. Zhong, B. Lu, Y. Wang, T. H. Cheung, and Y.-H. Liu, "Robot-enabled uterus manipulator for laparoscopic hysterectomy with soft RCM constraints: Design, control, and evaluation," *IEEE Trans. Med. Robot. Bionics*, vol. 4, no. 3, pp. 656–666, Aug. 2022.

[5] J. Wang, C. Lu, Y. Lv, S. Yang, M. Zhang, and Y. Shen, "Task space compliant control and six-dimensional force regulation toward automated robotic ultrasound imaging," *IEEE Trans. Autom. Sci. Eng.*, early access, Jun. 12, 2023, doi: 10.1109/TASE.2023.3282974.

[6] J. A. Klungsøyr, T. Vagstad, M. Ferle, J. O. Drogset, S. R. Hoff, A. F. Dalen, C. Hurschler, C. von Falck, and P. Klungsøyr, "The novel arthroscopic subscapular quadriceps tendon–bone sling procedure provides increased stability in shoulder cadavers with severe glenoid bone loss," *Knee Surgery, Sports Traumatol., Arthroscopy*, vol. 29, no. 1, pp. 170–180, Jan. 2021.

[7] M. Wellmann, H. de Ferrari, T. Smith, W. Petersen, C. H. Siebert, J. D. Agneskirchner, and C. Hurschler, "Biomechanical investigation of the stabilization principle of the Latarjet procedure," *Arch. Orthopaedic Trauma Surg.*, vol. 132, no. 3, pp. 377–386, Mar. 2012.

[8] C. W. Imhauser, R. N. Kent, J. Boorman-Padgett, R. Thein, T. L. Wickiewicz, and A. D. Pearle, "New parameters describing how knee ligaments carry force in situ predict interspecimen variations in laxity during simulated clinical exams," *J. Biomech.*, vol. 64, pp. 212–218, Nov. 2017.

[9] T. Vagstad, P. J. Klungsøyr, J. O. Drogset, D. Nebel, M. Ferle, C. Hurschler, and J. A. Klungsøyr, "The novel arthroscopic subscapular sling procedure grants better stability than an arthroscopic bankart repair in a cadaveric study," *Knee Surgery, Sports Traumatology, Arthroscopy*, vol. 28, no. 7, pp. 2316–2324, Jul. 2020.

[10] D. J. Goertzen and G. N. Kawchuk, "A novel application of velocity-based force control for use in robotic biomechanical testing," *J. Biomech.*, vol. 42, no. 3, pp. 366–369, Feb. 2009.

[11] T. Mae, K. Shino, T. Miyama, H. Shinjo, T. Ochi, H. Yoshikawa, and H. Fujie, "Single- versus two-femoral socket anterior cruciate ligament reconstruction technique: Biomechanical analysis using a robotic simulator," *Arthroscopy J. Arthroscopic Rel. Surg.*, vol. 17, no. 7, pp. 708–716, 2001.

[12] G. A. Livesay, H. Fujie, S. Kashiwaguchi, D. A. Morrow, F. H. Fu, and S. L.-Y. Woo, "Determination of thein situ forces and force distribution within the human anterior cruciate ligament," *Ann. Biomed. Eng.*, vol. 23, no. 4, pp. 467–474, Jul. 1995.

[13] L. D. Noble, R. W. Colbrunn, D.-G. Lee, A. J. van den Bogert, and B. L. Davis, "Design and validation of a general purpose robotic testing system for musculoskeletal applications," *J. Biomech. Eng.*, vol. 132, no. 2, Jan. 2010.

[14] C. Hurschler, N. Wülker, and M. Mendila, "The effect of negative intraarticular pressure and rotator cuff force on glenohumeral translation during simulated active elevation," *Clin. Biomech.*, vol. 15, no. 5, pp. 306–314, Jun. 2000.

[15] H. Fujie, K. Mabuchi, S. L.-Y. Woo, G. A. Livesay, S. Arai, and Y. Tsukamoto, "The use of robotics technology to study human joint kinematics: A new methodology," *J. Biomech. Eng.*, vol. 115, no. 3, pp. 211–217, Aug. 1993.

[16] H. Fujie, "Forces and moments in six-DOF at the human knee joint: Mathematical description for control," *J. Biomech.*, vol. 29, no. 12, pp. 1577–1585, Dec. 1996.

[17] T. W. Rudy, G. A. Livesay, S. L.-Y. Woo, and F. H. Fu, "A combined robotic/universal force sensor approach to determine in situ forces of knee ligaments," *J. Biomech.*, vol. 29, no. 10, pp. 1357–1360, Oct. 1996.

[18] L. G. Gilbertson, T. C. Doehring, and J. D. Kang, "New methods to study lumbar spine biomechanics: Delineation of in vitro load-displacement characteristics by using a robotic/UFS testing system with hybrid control," *Operative Techn. Orthopaedics*, vol. 10, no. 4, pp. 246–253, Oct. 2000.

[19] H. Martínez, "Development of a high-performance-6-DoF biomechanical joint analysis system based on an industrial robot," Ph.D. dissertation, Faculty Mech. Eng., Tech. Univ. Munich, München, Germany, 2012.

[20] M. T. Goldsmith, S. D. Smith, K. S. Jansson, R. F. LaPrade, and C. A. Wijdicks, "Characterization of robotic system passive path repeatability during specimen removal and reinstallation for in vitro knee joint testing," *Med. Eng. Phys.*, vol. 36, no. 10, pp. 1331–1337, Oct. 2014.

[21] H. El Daou, B. Lord, A. Amis, and F. Rodriguez y Baena, "Assessment of pose repeatability and specimen repositioning of a robotic joint testing platform," *Med. Eng. Phys.*, vol. 47, pp. 210–213, Sep. 2017.

[22] M. T. Goldsmith, M. T. Rasmussen, T. L. Turnbull, C. A. C. Trindade, R. F. LaPrade, M. J. Philippon, and C. A. Wijdicks, "Validation of a six degree-of-freedom robotic system for hip in vitro biomechanical testing," *J. Biomech.*, vol. 48, no. 15, pp. 4093–4100, Nov. 2015.

[23] H. El Daou, K. C. G. Ng, R. Van Arkel, J. R. T. Jeffers, and F. R. Y. Baena, "Robotic hip joint testing: Development and experimental protocols," *Med. Eng. Phys.*, vol. 63, pp. 57–62, Jan. 2019.

[24] M. Rychlik, G. Wendland, M. Jackowski, R. Rennert, K.-D. Schaser, and J. Nowotny, "Calibration procedure and biomechanical validation of an universal six degree-of-freedom robotic system for hip joint testing," *J. Orthopaedic Surg. Res.*, vol. 18, no. 1, p. 164, Mar. 2023.

[25] C. Hurschler, N. Wülker, H. Windhagen, P. Plumhoff, and N. Hellmers, "Medially based anterior capsular shift of the glenohumeral joint: Passive range of motion and posterior capsular strain," *Amer. J. Sports Med.*, vol. 29, no. 3, pp. 346–353, May 2001.

[26] C. Hurschler, "Experimental methods for the investigation of the biomechanics of the shoulder," Ph.D. dissertation, Medizinischen Hochschule Hannover, Hanover, Germany, 2004.

[27] S. Schröter, M. Krämer, B. Welke, C. Hurschler, R. Russo, M. Herbst, U. Stöckle, A. Ateschrang, and M. Maiotti, "The effect of the arthroscopic augmentation of the subscapularis tendon on shoulder instability and range of motion: A biomechanical study," *Clin. Biomechanics*, vol. 38, pp. 75–83, Oct. 2016.

[28] M. Schulze, R. Hartensuer, D. Gehweiler, U. Hölscher, M. J. Raschke, and T. Vordemvenne, "Evaluation of a robot-assisted testing system for multisegmental spine specimens," *J. Biomech.*, vol. 45, no. 8, pp. 1457–1462, May 2012.

[29] M. Ferle, "The soft-tissue restraints of the knee and its balancing capacity in total knee arthroplasty procedures," Ph.D. dissertation, Institutionelles Repositorium der Leibniz Universität Hannover, Hannover, Germany, 2020.

[30] S. L. Bokshan, S. F. DeFroda, J. A. Gil, R. Badida, J. J. Crisco, and B. D. Owens, "The 6-O'clock anchor increases labral repair strength in a biomechanical shoulder instability model," *Arthroscopy, J. Arthroscopic Rel. Surg.*, vol. 35, no. 10, pp. 2795–2800, Oct. 2019.

[31] (Apr. 2023). *About SimVITRO*. [Online]. Available: https://web.archive.org/web/20230408135727/https

[32] A. F. Dalen, M. G. Gregersen, A. L. Skrede, Ø. Bjelland, T. Å. Myklebust, F. A. Nilsen, and M. Molund, "Effects of progressive deltoid ligament sectioning on Weber b ankle fracture stability," *Foot Ankle Int.*, vol. 44, no. 9, pp. 895–904, Sep. 2023.

[33] K. C. Lynch and F. C. Park, *Modern Robotics: Mechanics, Planning, and Control*, 3rd ed. Cambridge, U.K.: Cambridge Univ. Press, 2019.

[34] M.-X. Kong, C. Ji, Z.-S. Chen, and R.-F. Li, "Application of orientation interpolation of robot using unit quaternion," in *Proc. IEEE Int. Conf. Inf. Autom. (ICIA)*, Aug. 2013, pp. 384–389.

[35] D. Q. Huynh, "Metrics for 3D rotations: Comparison and analysis," *J. Math. Imag. Vis.*, vol. 35, no. 2, pp. 155–164, Oct. 2009.

[36] P. Beeson and B. Ames, "TRAC-IK: An open-source library for improved solving of generic inverse kinematics," in *Proc. IEEE-RAS 15th Int. Conf. Humanoid Robots (Humanoids)*, Nov. 2015, pp. 928–935.

[37] S. G. Vougioukas, "Bias estimation and gravity compensation for force-torque sensors," in *Proc. 3rd WSEAS Symp. Math. Methods Comput. Techn. Electr. Eng.*, Dec. 2001, pp. 82–85.

[38] M. Krämer, A. Bäunker, M. Wellmann, C. Hurschler, and T. Smith, "Implant impingement during internal rotation after reverse shoulder arthroplasty. The effect of implant configuration and scapula anatomy: A biomechanical study," *Clin. Biomech.*, vol. 33, pp. 111–116, Mar. 2016.

[39] M. Adolphe, J. Clerval, Z. Kirchof, R. Lacombe-Delpech, and B. Zagrodny, "Center of mass of human's body segments," *Mech. Mech. Eng.*, vol. 21, no. 3, pp. 485–497, 2017.

[40] K. Sever, I. Indir, I. Vnucec, and J. Loncar, "Evaluation of gradient descent algorithm for attitude estimation," in *Proc. Int. Symp. ELMAR*, Sep. 2021, pp. 131–134.

[41] S. Marsland, *Machine Learning: An Algorithmic Perspective*, 2nd ed. Boca Raton, FL, USA: CRC Press, 2015.

[42] J. P. Iannotti, S. B. Lippitt, and G. R. Williams, "Variation in neck-shaft angle: Influence in prosthetic design," *American J. Orthopedics*, vol. 36, no. 12, pp. 9–14, 2007.

ALEKSANDER SKREDE (Graduate Student Member, IEEE) received the B.Sc. degree in automation and the M.Sc. degree in simulation and visualization from the Norwegian University of Science and Technology (NTNU), in 2014 and 2017, respectively, where he is currently pursuing the Ph.D. degree in robotics with the Department of ICT and Natural Sciences. He has been leading the technical development of Ålesund Biomechanics Laboratory (ÅBL), since 2018. He continues to develop the robotics infrastructure with ÅBL, NTNU. His research interests include robotics, optimization methods, state and parameter estimation, software architectures, and didactics.

ANDREAS FAGERHAUG DALEN received the M.D. degree from the Norwegian University of Science and Technology (NTNU), in 2013. He is currently pursuing the Ph.D. degree in orthopedics. He is also an Orthopedic Surgeon with Ålesund General Hospital. His research is focused on ankle fractures and biomechanics, working with Ålesund Biomechanics Laboratory (ÅBL), where he has been the Head, since 2018. His research interests include biomechanics and treatment of injuries in shoulders, knees, and ankles.

ALF INGE HELLEVIK received the M.D. and Ph.D. degrees from the Norwegian University of Science and Technology (NTNU), Trondheim, Norway, in 2010 and 2018, respectively. He is currently an orthopedic surgeon with Ålesund General Hospital and is also part of Ålesund Biomechanics Laboratory. His research interests include information design and visualization in medicine and surgery.

ØYVIND STAVDAHL (Member, IEEE) received the M.Sc. and Ph.D. degrees from the Department of Engineering Cybernetics, Norwegian University of Science and Technology (NTNU), Trondheim, Norway, in 1994 and 2002, respectively. In 1998. he joined the Department of Applied Cybernetics, SINTEF, as a Research Scientist, and became a Senior Scientist and the Head of the Motion Control Research Group, in 2004. Later, he returned to the Department of Engineering Cybernetics, NTNU, where he became an Associate Professor, in 2008, and a Professor, in 2018. His research interests include rehabilitation technology and biomimetics.

ROBIN T. BYE (Senior Member, IEEE) received the B.Eng. (Hons.), M.Eng.Sc., and Ph.D. degrees in electrical engineering from The University of New South Wales, Sydney, Australia, in 2004, 2005, and 2009, respectively. Since 2008, he has been with the Department of ICT and Natural Sciences (IIR), Norwegian University of Science and Technology (NTNU), Ålesund, and became a Professor, in 2020. He heads the Undergraduate Engineering Programme in Automation and Intelligent Systems and the Cyber-Physical Systems Laboratory, IIR. His research interests include cybernetics, artificial intelligence, neuroengineering, and engineering education. He was awarded the Goodeve Medal, in 2019.

• • •